

Where do the disks of spiral galaxies end?

J. Bland-Hawthorn

Anglo-Australian Observatory, P.O. Box 296, Epping, NSW 2121, Australia

K.C. Freeman & P.J. Quinn¹

Mt. Stromlo & Siding Springs Observatories, The Australian National University, Private Bag, Weston Creek P.O., ACT 2611, Australia

ABSTRACT

In spiral galaxies, the HI surface density declines with increasing radius to a point where it is seen to truncate dramatically in the best observed cases. It was anticipated that if the ambient radiation field is sufficiently strong, there exists a maximum radius beyond which the cold gas is unable to support itself against ionization. We have now succeeded in detecting ionized gas beyond the observed HI disk in spirals. Here, we report on our findings for the Sculptor galaxy NGC 253. The HI disks in Sculptor galaxies extend to only about $1.2 R_{25}$ although we have detected ionized gas to the limits of our survey out to $1.4 R_{25}$. This has important ramifications for spiral galaxies in that it now becomes possible to trace the gravitational potential beyond where the HI disk ends. The detections confirm that the rotation curve continues to rise in NGC 253, as it appears to do for other Sculptor galaxies from the HI measurements, but there is a hint that the rotation curve may fall abruptly not far beyond the edge of the HI disk. If this is correct, then it suggests that the dark halo of NGC 253 may be truncated near the HI edge, and provides further support for the link between dark matter and HI. The line ratios are anomalous with $[\text{NII}]\lambda 6548$ to $\text{H}\alpha$ ratios close to unity. While metallicities at these large radii are uncertain, such enhanced ratios compared to solar-abundance HII regions ($[\text{NII}]\lambda 6548/\text{H}\alpha = 0.05 - 0.2$) are likely to require selective heating of the electron population without further ionization of N^+ . We discuss the most likely sources of ionization and heating, and the possible role of refractory element depletion (e.g. Ca, Si, Fe) onto dust grains.

Subject headings: galaxy dynamics – dark matter – intergalactic medium – techniques: interferometric – techniques: spectroscopic

1. Introduction.

The case for dark matter in galaxies rests primarily on those spiral galaxies where the HI rotation curve has been measured at radii which are several times larger than the optical disk. At these large radii, the observed rotation of the gas is fully a factor of two larger than that expected for circular orbits in the

¹ *Current Address:* European Southern Observatory, Karl-Schwarzschild-Strasse 2, 85748 Garching bei München, Germany

potential field of the luminous galaxy (van Albada *et al.* 1985). Many of these extensive rotation curves are flat or even rising at the outermost points which means the edge of the mass distribution has not yet been found (Puche & Carignan 1991). In an attempt to find the edge, several observers have pushed their HI observations to higher sensitivity (van Gorkom 1993; Corbelli *et al.* 1989). These observations have shown that HI disks are abruptly truncated at column densities near 10^{19} atoms cm^{-2} where the rotation curves are still flat.

One possible explanation for the truncation is that, at large radii, the thin HI disks become fully ionized by the metagalactic UV background (Bochkarev & Sunyaev 1977). If this is the case, the outer parts of gaseous disks should be emitting $\text{H}\alpha$ photons. Maloney (1993) has shown that the expected $\text{H}\alpha$ emission measure from the ionized disk beyond the truncation point falls in the range $0.025\text{--}0.25 \text{ cm}^{-6} \text{ pc}$. After demonstrating that these flux levels are quite feasible with the TAURUS-2 Fabry-Perot interferometer (Bland-Hawthorn *et al.* 1994, hereafter BTVS), we now use this technique to search for the signature of ionized gas at and beyond the HI edge in Sculptor spirals.

The implications of a positive detection are profound. If the outer disk could be detected, then we would firstly know how extensive galactic disks (and dark haloes) really are and, secondly, we could continue tracking the rotation curve in order to find the edge of the halo and hence find the total mass of galaxies. A positive detection also has important implications for explaining low redshift $\text{Ly}\alpha$ absorption-line systems towards quasars, and for constraining the poorly known metagalactic ionizing background.

In §2, we describe the observations carried out at the AAT. In §3, we derive the expected level of $\text{H}\alpha$ emission at an HI edge, and then describe the experimental procedure to achieve such faint detections. The reduction and analysis steps are briefly outlined in §4, the results of which are discussed in §5. In §6, we attempt a physical interpretation of both the gas kinematics and the gas excitation before drawing our conclusions in §7.

2. Observations.

The observations were carried out over three long dark nights (1994 Aug 9–12) at the f/7.91 Cassegrain focus of the AAT 3.9m. Follow-up observations were carried out at f/14.9 on 1995 Sep 27. The TAURUS-2 interferometer was used in conjunction with the refurbished HIFI $40\mu\text{m}$ gap Queensgate etalon and a 4-cavity blocking filter (90% peak transmission), centered at $\lambda 6555\text{\AA}$, with a 45\AA bandpass well matched to the etalon free spectral range (54.3\AA at $\text{H}\alpha$). The 50mm filter was placed out of focus close to the focal plane and baffled to give a $5.0'$ field. The etalon was tilted by 3.4° to shift the optical axis to the field edge. An in-focus, focal plane, colander mask was used to ensure that low-order ghosts fall outside the field of view. The TAURUS-2 f/8 pupil diameter is 59.9mm which is oversized for the the 50mm diameter etalon. Due to uncertainties of the precise location of the optical cavity within the etalon, we placed a 45.0mm aperture stop immediately in front of the etalon. The pupil stop introduced a major loss of light (50%) compounded by a Cassegrain hole which is 17% of the total pupil area. The full pupil was used in the f/15 observations. The observational set-up was the same except for a 75mm blocking filter centered at 6585\AA which was not baffled thereby producing a field of view similar to the f/8 observations.

Observations were made at four positions in NGC 253 (Plates 1 and 2) with several discrete tunings of the etalon at each position (Table 1). The etalon was used at fixed gap spacings and the resulting ring pattern was imaged onto a Tek 1024² CCD with pixel scales of $0.594'' \text{ pix}^{-1}$ (f/8) and $0.315'' \text{ pix}^{-1}$ (f/15)

with read noise $\approx 2.3e^-$. The wavelength range $\lambda\lambda 6550 - 6590$ is dispersed quadratically over the $5'$ field at 1\AA resolution with blue wavelengths to the north. The instrument and detector were rotated to a position angle of 230° to align the detector with the galaxy major axis. At both foci, we observed two stellar flux standards (Table 1); at $f/8$, we also observed four planetary nebulae. Observations were also made of blank fields and in the direction of the Smith high velocity cloud (Smith 1963; Wakker 1991), and twilight flats were taken on all nights with and without the etalon.

3. Experiment

3.1. The expected H α flux

We now derive the expected flux levels from spiral edges ionized by a metagalactic radiation field. The surface density of HI gas falls exponentially in spiral galaxies. A point is reached where the HI column is no longer able to support itself against ionization by the cosmic radiation field. A naïve calculation can be used to predict the expected column density N_H at which this is likely to occur, in addition to the local electron density, n_e , and the expected emission measure, \mathcal{E}_m . More sophisticated treatments are given in Maloney (1993) and Dove & Shull (1994).

We shall assume that, at large galactocentric radius, the ionization rate is in rough equilibrium with the rate of recombination. Therefore, along an axis z perpendicular to the galactic disk, we find

$$2\alpha_B \int_0^\infty n_e n_p dz = \int_{\nu_o}^\infty \frac{4\pi J_\nu}{h\nu} d\nu \quad (1)$$

where the recombination coefficient α_B depends on the neutral hydrogen column and the local electron temperature (Case B: $\alpha_B \approx 2 \times 10^{-13} \text{ cm}^3 \text{ s}^{-1}$ at $T_e = 10^4\text{K}$). The local electron density n_e (and therefore the proton density n_p), is related to the neutral hydrogen density, n_H , through the ionizing fraction χ such that $n_e = \chi n_H$. Equation 1 assumes that the neutral gas sheet is ionized from both sides. We approximate the cosmic ionizing flux level as

$$J_\nu = 10^{-21} J_{-21}^o \left(\frac{\nu_o}{\nu}\right)^\beta \text{ erg cm}^{-2} \text{ s}^{-1} \text{ Hz}^{-1} \text{ sr}^{-1} \quad (2)$$

where J_{-21}^o is the metagalactic flux at the Lyman limit ($\nu = \nu_o$) in units of $\text{erg cm}^{-2} \text{ s}^{-1} \text{ Hz}^{-1} \text{ sr}^{-1}$. If the cosmic ionizing field (e.g. Haardt & Madau 1996) is due largely to quasars at high redshift, β is approximately unity.

For an exponential disk with density profile $n_H = n_H^o \exp(-z/z_s)$, the electron density in the plane of the galaxy at the ionized edge is

$$n_H^o \approx 1.8 \chi^{-1} \sqrt{J_{-21}^o (z_s \beta)^{-1}} \text{ cm}^{-3} \quad (3)$$

where the vertical scale height of the disk z_s is in parsecs. We assume a value of $z_s = 100 \text{ pc}$ throughout. The particle column density perpendicular to the disk is

$$N_H = 2 \int_0^\infty n_H dz \quad (4)$$

$$\approx 1.1 \times 10^{19} \chi^{-1} \sqrt{J_{-21}^o z_s \beta^{-1}} \text{ cm}^{-2}. \quad (5)$$

For a 2σ upper limit of $J_{-21}^o = 0.08 \text{ erg cm}^{-2} \text{ s}^{-1} \text{ Hz}^{-1} \text{ sr}^{-1}$ (Vogel *et al.* 1995; Bland-Hawthorn 1997), the gas is fully ionized when $n_{\text{H}}^o \approx 0.05 \text{ cm}^{-3}$ and $N_{\text{H}} \approx 3 \times 10^{19} \text{ cm}^{-2}$. The latter is in good agreement with observations (e.g. Corbelli *et al.* 1989). A crude upper limit on the $\text{H}\alpha$ emission measure \mathcal{E}_m is

$$\mathcal{E}_m = \int n_e n_p \text{ dl} \approx 0.25 \text{ cm}^{-6} \text{ pc.} \quad (6)$$

This surface brightness, equivalent to 90 milliRayleighs (mR) and $5 \times 10^{-19} \text{ erg cm}^{-2} \text{ s}^{-1} \text{ arcsec}^{-2}$, is reached at the 3σ level by the Fabry-Perot ‘staring’ technique in less than one hour of observation (BTVS).²

3.2. Fabry-Perot ‘staring’

We exploit the ‘staring’ technique to obtain a single, extremely deep spectrum of a diffuse source which fills the field of view. For a fixed gap spacing, $\lambda \propto \cos \theta$ where θ is the angle of an incoming ray of wavelength λ to the optical axis. The spectrum in a narrow band ($\sim 40\text{\AA}$) is dispersed radially from the optical axis across the field (see Fig. 3). Like long-slit spectrometers, the instrumental profile is projected onto the detector but the line FWHM in pixels varies across the field inversely with θ . Complete Fabry-Perot rings have constant surface brightness and equal spectroscopic resolution. After flatfielding and point source removal, the data are binned azimuthally and resampled to a linear axis to obtain a single deep spectrum (e.g. Figs. 4 and 5).

Maximum sensitivity is achieved when (a) the detector covers the unvignetted field, (b) the line-emitting source fills the field of view, and (c) the velocity range and internal kinematic dispersion, taken together, are comparable to the instrumental profile width. These criteria determine which galaxies are best matched to a given instrument.

The isovelocity contours of a disk undergoing flat rotation show two distinct regimes. The central region of solid body rotation gives rise to contours which are parallel to the kinematic minor axis. At the turnover radius, the contours become radial and therefore subtend a fixed angle as seen on the sky about the kinematic major axis. The spread in velocity within a fixed field of view declines inversely with radius until we reach the intrinsic spread of an isothermal HI disk ($\sigma_{\text{HI}} \approx 10 \text{ km s}^{-1}$; Kamphuis 1993). An important concept is the angular extent of the “innermost monochromatic field” (imf) for a given instrument, telescope and object. We define this as the field at the smallest radius along the disk major axis within which the observed spread in velocities does not exceed the instrumental resolution. The necessary condition for a galaxy with maximum deprojected velocity v_{max} inclined at an angle i is

$$\frac{1}{4} v_{\text{max}}^2 \sin^2 i \left[1 + \left(\frac{\mu F_{\text{kpc}}}{2R \sin i} \right)^2 \right]^{-1} + \sigma_{\text{HI}}^2 \leq \sigma_{\text{FP}}^2 \quad (7)$$

where σ_{FP} is the instrumental width (in km s^{-1}) and R is the radius to the field center (in kpc). Truncated HI edges typically occur at radii larger than the semi-major axis distance (R_{25} in kpc) of the $B = 25$ mag arcsec^{-2} contour. For a fixed field F_{kpc} (in kpc), this condition is most easily satisfied in large, nearby galaxies where the instrument field of view is a small fraction of the object size. The constant μ

²1 Rayleigh is $10^6/4\pi \text{ phot cm}^{-2} \text{ s}^{-1} \text{ sr}^{-1}$ or $2.41 \times 10^{-7} \text{ erg cm}^{-2} \text{ s}^{-1} \text{ sr}^{-1}$ at $\text{H}\alpha$.

allows for two different approaches to sky subtraction. If this is achieved through a separate exposure, $\mu = 1$; otherwise, in a properly matched experiment, we assume that half the field is given over to the sky background for which $\mu = 0.5$.

The optimal disk inclination is unclear: face-on galaxies have a smaller velocity spread and subtend larger solid angles, whereas an inclined disk has a higher projected column density. A potential problem in edge-on disks is flaring due to the declining stellar surface density (Olling 1995) which tends to reduce the projected emission measure. To minimize the velocity spread, we rotate the instrument so that the incomplete ring pattern is convex in the same sense as the projected velocity field, and is centered on the kinematic major axis (see Figs. 1 and 2).

4. Reduction & Analysis

A detailed discussion of the many subtleties of data analysis are to be presented elsewhere; a brief overview is given here. An important step is establishing the optical axis of the incomplete calibration rings to better than 0.1 pix. This was achieved with orthogonal distance regression (e.g. Boggs, Byrd & Schnabel 1987). Next, we azimuthally bin the calibration rings for all nights to ensure that (a) there were no opto-mechanical shifts, (b) the instrumental response was constant, and (c) the etalon gap zero-point was constant from night to night. In (b), the etalon was found to behave reliably except that there was a slow drift in the optical gap during the first night.

Some calibration spectra showed baseline variations after binning over different parts of the field. This arises from illumination (vignette) effects, stray light, chip structure and CCD fringeing which can be divided out reliably with flatfields. The spectral bandpass seen by individual pixels is roughly 1\AA where the bandpass centroid declines by 40\AA from the optical axis to the field edge. Twilight flats were found to be the most reliable except that the Fraunhofer spectrum leaves its imprint in the data. We divide out the solar spectrum from the flatfield by establishing the mean spectrum and then generating a polar image with this spectrum. Occasionally, the flatfields leave residual fringe structure in the data. It is possible to remove this with azimuthal smoothing but potentially informative, intensity variations in the data will be washed out. CCD fringeing constitutes the main systematic error in diffuse detection and provides a major challenge to achieving deeper detection limits than that quoted by BTVS. The response of the blocking filter is removed in the twilight division.

To obtain discrete spectra from the summed CCD images, the data were divided into annular rings two pixels wide. Within each annulus, we can calculate the mean, median or mode of the histogram. Cosmic ray events appear as outliers and are therefore easily removed. We tried more sophisticated methods (e.g. the bi-weight statistic) but the improvement was found to be marginal. The weak underlying galaxy continuum observed in NGC 253 had only a negligible effect on the final spectra. This was examined by subtracting a matching R band exposure modulated by the polar response of the blocking filter. This same image was used to identify unresolved sources within the field.

Sky subtraction is particularly hazardous since atmospheric humidity produces variable water vapour features. If the object fills the field of view, as for NGC 253, it is necessary to obtain off-field exposures at the same airmass and at comparable humidity. The OH lines are time variable but, most importantly, they vary with the zenith angle of the observation (Kondratyev 1969). This is quite distinct from the geocoronal lines which reach a minimum at local midnight rising sharply towards dawn. The night sky lines allow for

wavelength calibration to better than 0.04\AA (Osterbrock & Martel 1992) as shown by the difference in wavelength produced by a discharge lamp and solar $\text{Ly}\beta$ resonance excitation of the exosphere (Yelle & Roesler 1985). The velocity centroid of the galactic $[\text{NII}]$ emission (‘Reynolds layer’), using new wavelengths from Spyromilio (1995), provides an independent measurement of the Earth-Sun motion with respect to the Local Standard of Rest. For all four nights, the conditions were consistently photometric as judged by the Reynolds layer emission. The photometric calibration was achieved using both line and continuum flux standards (Table 1).

5. Results

The four TAURUS-2 field positions are shown in Figs. 1 and 2 overlaid on a B image of NGC 253 and the deepest HI image to date for this galaxy. A magnified section of one interferogram is shown in Fig. 3 and summed spectra are shown for the two outermost fields in Figs. 4 and 5. The ‘staring’ method allows for an extremely deep spectroscopic detection over pixels that fall within the projected arc defined by a discrete frequency. There are two frequencies of interest so that kinematic measurements are possible at two positions within each field. The etalon was tuned to two different spacings for the two innermost fields so that we have kinematic measurements at no more than 12 independent positions along the major axis. These data are presented in Figs. 6 and 7.

Optical line emission is detected in all field positions. In fields SW1 and SW2, bright HII regions were clearly seen in both $\text{H}\alpha$ and $[\text{NII}]\lambda 6548$. These short exposures were taken to establish independently the systemic velocity of the gas. The kinematic measurements are seen in Fig. 6c at $r < 7'$. The large systematic errors in both axes are due to azimuthally averaging over a large spread in velocities and radial distances within the projected plane at small galaxian radii.

Field SW3 is the imf defined by the criterion in equation 7. Weak stellar continuum emission is seen over the central third of the field extending from roughly $\mu_B = 23 \text{ mag arcsec}^{-2}$ (NE) to $25 \text{ mag arcsec}^{-2}$ (SW). The $[\text{NII}]$ and $\text{H}\alpha$ line emission comprise clumpy structure superimposed on a faint diffuse component. Only two of the sources are unresolved: these show up on our matched BVR images and are labelled in Fig. 3. The two bright knots at the position of the $[\text{NII}]$ line are probably faint HII regions.

The summed spectrum for field SW3 is shown Fig. 4. The difference of the on-object and off-object spectra clearly shows the declining stellar disk along the major axis, in addition to the $[\text{NII}]$ and $\text{H}\alpha$ lines at 6557.7\AA and 6572.8\AA . While these lines fall at different spatial locations within the galaxy, the strength of the blue $[\text{NII}]$ line with respect to $\text{H}\alpha$ is striking, a result which holds after removing the bright knots. The weakness of the galaxy continuum rules out a significant correction to the $\text{H}\alpha$ line flux due to stellar absorption (Bica & Alloin 1987). We achieved the same basic result in the 1995 September 27 observations although the signal-to-noise ratio was roughly half that of the earlier observations. Both sets of observations show that the diffuse emission peaks towards the major axis.

The summed spectrum for field SW4 is presented in Fig. 5. This field lies beyond the HI edge of NGC 253. Unfortunately, we did not manage to obtain a matching sky observation. The data clearly show weak $[\text{NII}]$ emission and possibly broad diffuse $\text{H}\alpha$ emission. We have attempted to subtract something approximating a background spectrum by dividing up the field into three vertical panels which have equal area when the outer panels are taken together. The central section constitutes our on-object spectrum, the outer quarter panels our off-object spectrum. The weak outer envelope of the galaxy is seen in the

difference spectrum. The [NII] emission peaks towards the major axis and is not detected in the outermost panels. Broad diffuse H α emission is seen in both regions at comparable intensity and therefore subtracts cleanly in the residual spectrum. That this feature is real can be seen by comparing the lower spectrum in Fig. 5 with the off-object spectrum in Fig. 4 where such a feature is not seen.

The radial velocities for the emission lines in Figs. 4 and 5 were corrected for the Earth’s motion before subtracting the systemic velocity of NGC 253. These measurements are presented in Figs. 6 and 7. The innermost TAURUS-2 measurements were used to establish the systemic velocity of the ionized gas. Schommer *et al.* (1993) show the systematic uncertainties which can arise between HI and ionized gas kinematics. Our optical determination ($243 \pm 9 \text{ km s}^{-1}$) is consistent with the weighted-average HI measurements ($249 \pm 8 \text{ km s}^{-1}$) from the NASA/IPAC Extragalactic Database. We adopt the HI value $245 \pm 5 \text{ km s}^{-1}$ (Puche *et al.* 1991, hereafter PCvG) as we wish to relate the optical data to their data. For the measurements between $r = 10'$ and $r = 14'$, the kinematic error is dominated by the uncertainty in systemic velocity. The smaller error bars compared to the inner TAURUS-2 measurements reflect the smaller intrinsic radial and kinematic dispersion. That the optical values appear systematically high by 10 km s^{-1} is discussed in the next section. For the outermost point, the diffuse broad feature has a large kinematic measurement uncertainty. Unlike the other lines, this feature has fairly uniform intensity over the full field. Its lack of continuity with the other measurements calls into question its association with the galaxy.

6. Discussion

6.1. Dynamical interpretation

The major axis measurements in NGC 253 pose an interesting problem. In Fig. 6, the “rotation curve” appears to flatten off before rising at a radius $r = 7'$. This effect is seen for both the approaching and receding sides of the disk, with (Fig. 6b) or without (Fig. 6a) the correction for orbit inclination. In Fig. 6c, the TAURUS-2 measurements confirm and extend this trend out to $r = 13'.5$. The outer TAURUS-2 values are somewhat higher than the azimuthally averaged HI rotation curve, but this is a distinctive feature of the approaching side of the disk (Fig. 6a) in that the outer HI measurements here are higher than average.

If we assume that the distribution of mass has spherical symmetry, then from Poisson’s equation,

$$\frac{d}{dr}(rv_c^2) = 4\pi Gr^2\rho(r) \quad (8)$$

where ρ and v_c are the local mass density and the circular velocity. For the flat region of v_c , ρ declines as r^{-2} ; the sudden rise requires the density profile to become much flatter or even constant with increasing radius. A slightly flattened potential gives the same result although the inferred total mass will be overestimated in this case.

The inflexion in the rotation curve can be understood naturally to arise from the potential of an exponential stellar disk with a much larger dark halo (e.g. Carignan & Freeman 1985). To illustrate this, we show a variety of possible 3-component fits to the data.

In the first model (Fig. 7a), the HI and stellar disks have the same form. The dark halo is represented by an isothermal sphere, which is fully specified by any two of the halo central density, ρ_h , the central

velocity dispersion σ_h , or the core radius r_h . The stellar disk is specified by a central surface density μ_e and a scale length r_e . The HI surface density profile is given in PCvG (Fig. 5); the central hole within $r = 1.9$ causes the gravitational force due to the gas to be directed outward (e.g. Staveley-Smith *et al.* 1990). We have taken $\sigma_h = 253 \text{ km s}^{-1}$, $r_h = 18 \text{ kpc}$, $\mu_e = 1.35 \times 10^9 M_\odot \text{ kpc}^{-2}$ and $r_e = 1.6 \text{ kpc}$. These values compare well with PCvG except that the disk and halo scale lengths are 30% smaller than their values. In order to match the observed data, the model rotation curves have been projected to a plane inclined at 72° . We note that such a large core radius is normal for the dark halo of large disk galaxies (e.g., Freeman 1993).

In the second model (Fig. 7b), the radial forms of the disk and halo are given by Dehnen & Binney (1997). For the halo, we adopt

$$\rho_h(R, z) = \rho_o \left(\frac{m}{r_o}\right)^{-g} \left(1 + \frac{m}{r_o}\right)^{g-b} \exp(-m^2/r_t^2) \quad (9)$$

with

$$m^2 = R^2 + (z/q)^2. \quad (10)$$

The halo parameters are the halo density normalization, ρ_o , the halo scale radius, r_o , the outer cut-off radius, r_t , and the inner and outer power slopes g and b . Apart from the halo axis ratio ($q = 0.8$), all of these parameters were obtained from a fit to the rotation curve. Both the stellar and gaseous disks are assumed to be exponential in form, i.e.

$$\rho_d(R, z) = \frac{\mu_d}{2z_d} \exp\left(-\frac{R_m}{R} - \frac{R}{R_d} - \frac{|z|}{z_d}\right). \quad (11)$$

For each of the disks, the adopted parameters are the surface density normalization, μ_d , the disk scale height, z_d , and the disk scale radius and inner cut-off radius, R_d and R_m . For the HI disk, these were fixed at $\mu_d = 1.94 \times 10^7 M_\odot \text{ kpc}^{-2}$, $R_d = 3.92 \text{ kpc}$, $z_d = 0.04 \text{ kpc}$, and $R_m = 1.22 \text{ kpc}$. For the stellar disk, $R_d = 1.80 \text{ kpc}$, $z_d = 0.15 \text{ kpc}$, and $R_m = 0 \text{ kpc}$ as suggested by the photometry. The surface density normalization for the stellar disk was obtained from the least-squares fit.

The fit, kindly undertaken by W. Dehnen, ignored the last TAURUS-2 measurement to yield the following results: $\mu_d = 1.56 \times 10^9 M_\odot \text{ kpc}^{-2}$, $\rho_o = 1.98 \times 10^8 M_\odot \text{ kpc}^{-3}$, $g = -1.058$, $b = 1$, $r_o = 34.2 \text{ kpc}$ and $r_t = 164.0 \text{ kpc}$. Of these, b was constrained to be greater than or equal to unity. Fig. 7b shows that the rising halo contribution to the rotation curve gives a better fit to the data overall. But there are strong correlations between the various parameters and the fitted results depend critically on which of the TAURUS-2 points are included.

The outermost TAURUS-2 $\text{H}\alpha$ measurement in Figs. 6c and 7 suggests that the rotation curve may be falling beyond a radius of about 10 kpc, but there are certainly other possible explanations for its low observed velocity. For example, (i) it may result from tidal distortion of the outermost regions of NGC 253, or (ii) from accretion of a faint gas-rich object at large radius. In support of the accretion idea, a stacked photographic image by D. Malin shows extended stellar light at faint levels ($\sim 26 \text{ mag arcsec}^{-2}$) to the SW of the disk; similar emission is not seen to the NE. (iii) While the emission may arise from an outer ionized envelope, it is conceivable that this emission is associated with the group itself. An extragalactic H^+ cloud has recently been discovered in the Fornax cluster (Bland-Hawthorn *et al.* 1995). Mathewson, Cleary & Murray (1975) and Arp (1985) found tentative evidence for HI clouds within the Sculptor group (cf. Haynes & Roberts 1979). It is difficult, however, to reconcile the $\text{H}\alpha$ radial velocity ($\approx 440 \text{ km s}^{-1}$) with the Magellanic Stream which passes in front of the Sculptor group (Mathewson & Ford 1984).

Finally, we consider the possibility that the rotation curve of NGC 253 is indeed falling beyond 10 kpc. Such a rapid decrease suggests that the dark halo may be truncated. We can illustrate the effect of such truncation with a simple model. We take the halo density distribution to be

$$\rho_h = \rho_o(1 + r^2/r_a^2)^{-1} \quad (12)$$

with the rotation curve $V(r)$ given by

$$V^2 = V_\infty^2 [1 - (\frac{r_a}{r}) \tan^{-1}(\frac{r}{r_a})] \quad (13)$$

For $V_\infty = 733 \text{ km s}^{-1}$ and core radius $r_a = 18 \text{ kpc}$, the rotation curve for this model is very similar to that of the isothermal halo in Fig. 7a: the optical galaxy lies well within the core radius of the halo, and the halo rotation curve is close to solid-body. We now truncate the halo at $r = 10 \text{ kpc}$; its rotation curve is then Keplerian for $r > 10 \text{ kpc}$. Fig. 7c shows how the resulting total rotation curve now provides an acceptable fit to all of the HI and TAURUS-2 data. The model is artificial (the halo is sharply truncated, and we did not truncate the stellar and HI disks), but the point is obvious enough: truncation of the dark halo near the observed outer edge of the HI disk can produce the apparent falling rotation curve.

If this is all correct so far, there are some interesting consequences. The properties of dark halos are best studied in disk galaxies for which the HI distribution extends well beyond the optical distribution. In the outer regions of these galaxies, the ratio of (dark matter surface density)/(HI surface density) is roughly constant (*e.g.*, Bosma, 1978; Carignan 1991). NGC 253 is not such a galaxy. Its HI extent is similar to its optical extent (*e.g.*, PCvG). Our data provides the first hint that, in galaxies like NGC 253 where the HI and the light are co-extensive, the dark matter also may not extend much beyond the optical distribution. It is tentative evidence of the apparent link between the dark matter and the HI. We emphasize that the dark matter is still essential to generate the observed rotation curve for NGC 253: the inferred mass ratio of dark matter to luminous matter is about 5. Our point is simply that the dark matter distribution in NGC 253 may be truncated at a radius of only 10 kpc, compared to the much larger dark halo distributions observed in our Galaxy (*e.g.*, Freeman 1996) and other large spirals (*e.g.*, Zaritsky *et al.* 1997).

The reduced chi square for the models presented in Fig. 7a and 7b are 5.2 and 2.9 respectively. The latter model has the highest statistical significance of all models, but the basic assumptions are unlikely to be physical. A flat rotation curve given by equation 13 does not fit the measurements adequately. The reduced chi square is 6.3 and, more significantly, 10 of 12 points outside of $r = 7'$ miss the curve by more than 2σ . But the inclusion of a truncation radius lowers the reduced chi square to 3.9 and the curve now passes through all the outer points (Fig. 7c).

6.2. Ionization and heating of the diffuse gas

The most striking feature of the spectra presented in Figs. 4 and 5 is the inferred high $[\text{NII}]\lambda 6548/\text{H}\alpha$ ratios. In order to ensure that the whitelight calibration adequately removed the filter response over the field (§4), we examined the line ratios in HII regions over the inner disk. Where we have two interference rings that fall close together on the sky – one from $\text{H}\alpha$, the other from $[\text{NII}]$ – the HII regions appear weak in $[\text{NII}]$ compared to $\text{H}\alpha$, indicative of the order of magnitude difference expected for inner disk HII regions. If the outer HI gas has sub-solar abundances (Pagel 1989; Diaz 1989), the enhanced line ratio must arise from one or more excitation processes. However, to date, numerical models involving a single ionizing

source have not managed to produce such an enhancement (e.g. Sokolowski 1994). Thus, we separate our discussion of ionization and excitation wherever possible. Almost certainly, the anomalous ratio is indicative of a higher local electron temperature for which there are various mechanisms. In solar-abundance HII regions, this ratio rarely exceeds 0.15 (Evans & Dopita 1985): to substantially increase this ratio requires that we selectively heat the electrons without producing N^{++} .

The required ionizing flux. The emission measure \mathcal{E}_m from the surface of a cloud embedded in a bath of ionizing radiation gives a direct gauge, independent of distance, of the intensity of the ambient radiation field beyond the Lyman continuum (Lyc) edge (e.g., Hogan & Weymann 1987). This assumes that the covering fraction *seen by the ionizing photons* is known and that there are sufficient gas atoms to soak up the incident ionizing photons. At electron temperatures of 10^4K , collisional ionization processes are negligible. Perpendicular to the surface, from equation 1, the column recombination rate in equilibrium must equal the incident ionizing photon flux, $\alpha_{\text{Bn}_e} N_p = \varphi_i$, where φ_i is the rate at which Lyman continuum photons arrive at a planar cloud surface ($\text{phot cm}^{-2} \text{s}^{-1}$), and N_p is the column density of ionized hydrogen. The emission measure produced by this ionizing flux is

$$\mathcal{E}_m \approx 4.5\varphi_4 \text{ mR} \tag{14}$$

where $\varphi_i = 10^4\varphi_4$ (Bland-Hawthorn & Maloney 1997, hereafter BM). For an optically thin cloud in an isotropic radiation field, the solid angle from which radiation is received is $\Omega = 4\pi$, while for one-sided illumination, $\Omega = 2\pi$. However, φ_i can be anisotropic and Ω can be considerably less than 2π .

Metagalactic ionizing background. The measured surface brightness values for the emission lines in Figs. 4 and 5 are as follows: for the $[\text{NII}]\lambda 6548$ line, $90\pm 5 \text{ mR}$ ($r = 10'5$), $46\pm 5 \text{ mR}$ ($r = 12'0$); for the $\text{H}\alpha$ line, $81\pm 6 \text{ mR}$ ($r = 13'5$), $41\pm 8 \text{ mR}$ ($r = 15'0$). If the underlying HI is optically thick to the Lyman continuum, the $\text{H}\alpha$ lines require an ionizing flux of $2 \times 10^5 \text{ phot cm}^{-2} \text{ s}^{-1}$ and $9 \times 10^4 \text{ phot cm}^{-2} \text{ s}^{-1}$. The present upper limit on the metagalactic ionizing flux (§3.1) is $J_{21}^{\circ} < 0.08 \text{ erg cm}^{-2} \text{ s}^{-1} \text{ Hz}^{-1} \text{ sr}^{-1}$ (2σ) which sets an upper limit on the one-sided ionizing flux at the surface of an optically thick HI sheet of $2 \times 10^4 \text{ phot cm}^{-2} \text{ s}^{-1}$, thereby ruling out the metagalactic background as the dominant ionizing source. The combined ionizing radiation from hot gas and galaxies within the Sculptor group is also much too weak. Sciama (1995) predicts an order of magnitude higher ionizing flux from decaying neutrinos which could conceivably account for much of the $\text{H}\alpha$ flux. However, the narrow energy bandpass of decaying neutrinos (Sciama 1996) at the Lyman limit cannot produce N^+ , and therefore requires an additional source of ionization.

Compact halo sources. The most recent summary of the MACHO project indicates that as much as half of the dark matter in the Galaxy out to the LMC is made up of solar mass objects. There is wide disagreement on whether the missing mass could comprise a halo population of white dwarfs (Adams & Laughlin 1996; Kawaler 1996; Chabrier, Segretain & Mera 1996). But most plausible models invoke a population which produces essentially no UV flux today. This is supported by high redshift observations of the precursor halo population (Charlot & Silk 1995).

Compact disk sources. Unlike ellipticals, spiral galaxy disks tend not to “grow” when photographic plates are stacked or amplified to reveal light at very faint levels (Malin 1983). But a photographically amplified plate of NGC 253 (Malin 1981) reveals a faint blue disk extending to the limits of our outermost detection ($r = 15'$). Following a suggestion from G.B. Field, we now consider whether these could comprise an extended white dwarf population (including the precursor population of central stars in planetary nebulae) young enough to produce a significant UV disk flux. Such a population was originally broached by Lyon (1975) and Bania & Lyon (1980). In Fig. 8, we consider whether white dwarfs are able to account for the diffuse line emission in concert with the faint stellar continuum at the HI edge in NGC 253 (barred

arrow). We present the expected $H\alpha$ emission measure \mathcal{E}_m versus B surface brightness for an isothermal population of white dwarfs as a function of the disk surface density. The contribution to both of these quantities from white dwarfs in the solar neighbourhood is also shown (filled symbols). The luminosity function is taken from Liebert, Dahn & Monet (1988) and the luminosity–temperature conversion from Wood (1990).

There are two basic problems in using white dwarfs to explain the disk ionization. In the solar neighbourhood, the combined effect of all white dwarfs could produce $\mathcal{E}_m = 0.1 \text{ cm}^{-6} \text{ pc}$ which fails to explain the Reynolds layer emission by an order of magnitude or more, in agreement with Nordgren, Cordes & Terzian (1992). If we assume a comparable star formation history in the outer reaches of NGC 253, this model could conceivably be used to explain the measured $H\alpha$ emission. This is particularly attractive in that the high temperatures of the white dwarf population produce elevated $[NII]/H\alpha$ ratios (Sokolowski & Bland-Hawthorn 1991). However, if the luminosity function resembles the solar neighbourhood, the combined disk surface brightness at B from the cooler white dwarfs is very much brighter than observed, particularly when one includes the contribution of early main sequence stars. Alternatively, attempting to explain the low $H\alpha$ emission measure in terms of 2000 white dwarfs kpc^{-2} at 45,000 K leads to a timing problem. We have measured an age–temperature relation from Wood (1990) for which

$$\log\left(\frac{t}{\text{yrs}}\right) = 3.6 \log T_{\text{wd}} - 9.7. \quad (15)$$

Stars hotter than 40,000 K have left the asymptotic giant branch less than 10^7 years ago which would require a highly contrived star formation history throughout the disk.

S.G. Ryan has suggested the possibility of hot horizontal branch stars, in particular, an isothermal population with temperatures around 15,000 K (Lee 1993). If we assume comparable line blanketing with white dwarfs, Fig. 8 illustrates that such a population will always produce too much blue light for the required ionizing flux, irrespective of the uncertain sizes and surface densities of both objects. The characteristic “temperature” of the ionizing source needs to be sufficiently high to fall within the strict B band limit. Interestingly, this is just what is needed to significantly enhance the $[NII]/H\alpha$ ratio as photons with higher mean energies produce higher electron temperatures.

Ram pressure heating. Mathis (1986) has stressed the problems associated with shocks as a source of ionization and heating for the Reynolds layer, particularly the near-uniformity of the emission. An interesting possibility is ram pressure heating as NGC 253 moves through an external medium where the disk is inclined at some angle to its direction of motion. The wake of NGC 7421 (Ryder *et al.* 1996) suggests that such a process can take place. To ionize a column of 10^{19} atoms cm^{-2} requires shock speeds close to 130 km s^{-1} (Dopita & Sutherland 1996). A medium with pre-shock density $\sim 10^{-2} \text{ cm}^{-3}$ moving through an ambient medium with the relatively high density $\sim 10^{-3} \text{ cm}^{-3}$ at 400 km s^{-1} could produce the necessary ram pressure. The post-shock temperature at a shock velocity of 130 km s^{-1} is $2.4 \times 10^5 K$ which is a factor of ten higher than the upper limit from the Doppler parameter (22 km s^{-1}) of the observed line profiles. For N^+ and H^+ to have been collisionally ionized, the gas must have had time to cool. But groups with low velocity dispersions, like the Sculptor group, tend to have very little intracluster medium (Fadda *et al.* 1996). Therefore, the galaxy would need to be running into a large, external gas cloud for the shock model to remain plausible.

Exotic heat sources. There exists a wide range of ‘exotic’ models for preferentially heating the electron population including turbulence-driven MHD wave heating (Raymond 1990), and mixing layers driven by bulk flows (Slavin, Shull & Begelman 1993). Bulk flows and turbulence in the disk are thought to be

maintained primarily by energy injection from star formation. The star formation rates at the HI edge are likely to be very small. An alternative possibility is that the outer disk is being rained on by galactic fountain material driven by the inner starburst (e.g. Benjamin & Shapiro 1993). It is unclear at present whether fountain models can generate the necessary heating through shocks. Ferland & Mushotsky (1984) have shown that under rather special conditions, low energy cosmic ray electrons can selectively heat ions and electrons through Coulomb repulsion. However, Sciama (1996) emphasizes the difficulties involved in cosmic rays penetrating gas clouds and these do not appear to be an important agent.

Young stellar disk. The inner disk of NGC 253 hosts a young, stellar population producing copious amounts of ionizing photons. It is plausible that the outer disk sees this radiation either through dust scattering or through warps in the outer parts. For Rayleigh scattering, we have repeated the calculations of Jura (1980) using up-to-date dielectric phase functions (Martin & Rouleau 1990; Draine & Lee 1984) and assuming a standard grain mixture and distribution (Mathis, Rumpl & Nordsieck 1977). We adopt the Henyey-Greenstein (1941) phase function which relates the asymmetry parameter g to photon energy. The expected ionizing flux at the HI edge is much less than 10^5 phot cm⁻² s⁻¹ due primarily to the highly forward-scattering behaviour ($g > 0.9$) of the grains at increasing energy towards the Lyman limit.

While there is some uncertainty as to the fraction of ionizing photons which escape a normal spiral galaxy, two independent lines of argument suggest that roughly 5% of ionizing photons escape the Galaxy (Domgörgen & Mathis 1994; BM). The absolute B magnitude of NGC 253 is comparable to that inferred for the Galaxy and thus, if the disk opacity is comparable in both cases, the same models in BM apply here. G.D. Bothun (personal communication) suspects that the disk of NGC 253 may be more opaque than the Milky Way, in which case our predicted fluxes should be considered upper limits. To explain the H α flux at both outer positions (9 and 12 kpc) requires an integral sign warp originating at 7 kpc reaching 20° at 10 kpc. It is difficult to rule this out on the basis of the HI data. At face value, Fig. 8 of PCvG indicates such a warp starts at 7 kpc reaching $\approx 10^\circ$ at 9 kpc. In the next section, we explore this model in more detail.

Dilute photoionization. After Sokolowski (1994), we attempt to simulate conditions at the HI edges of spiral galaxies ionized by the stellar radiation field from the central disk. This requires that the outer SW edge of NGC 253 is warped ($\sim 25^\circ$) or flares up and therefore sees the central regions. We use the CLOUDY code (Ferland 1991) to ionize plane parallel slabs with cosmic abundances (Grevesse & Anders 1989). The physical state and emission spectrum of a low-density photoionized gas with a given composition are fixed by two parameters – the shape of the ionizing continuum and the ionization parameter (Tarter, Tucker & Salpeter 1969). For the ionization parameter, U (the ratio of ionizing photons to nucleons), we adopt

$$U = \frac{\varphi}{cn_{\text{H}}} \quad (16)$$

where c is the speed of light. In Fig. 10, the results for a range of emission-line diagnostics are presented as a function U . The radiation-bounded models are truncated when the electron temperature T_e falls below 4000K; all models assume $n_{\text{H}} = 1 \text{ cm}^{-3}$.

The unabsorbed radiation field is a composite taking the form $\psi_c \xi(M_*) t(M_*)$ where ψ_c is the current star formation rate, ξ is the initial mass function, and t is the main-sequence lifetime. The ionizing field is dominated by stars with $M_* \geq 40M_\odot$; we specify the upper mass cut-off to be $M_* = 120M_\odot$. The stellar atmospheres are from Mihalas (1972) and Kurucz (1979); the solar metallicity evolutionary tracks are from Maeder (1990). For the massive star IMF, we adopt $\xi(M_*) \propto M_*^{-2.7}$ which falls between the Salpeter (1955) and the Miller-Scalo (1979) models.

Irrespective of the *shape* of the ionizing continuum, a dilute radiation field leads to enhanced emission

from low ionization emission lines (Ferland & Netzer 1983; Halpern & Steiner 1983). But a general hardening of the ionizing field also produces the same trend (e.g. Sokolowski & Bland-Hawthorn 1991). Indeed, if the edges of spirals are ionized by the central stellar disk, the ionizing field is expected to be both dilute and hardened.

There are at least two phenomena which serve to harden the local ionizing radiation field: interstellar opacity and metal depletion (i.e. refractory elements) onto grains. We assume that the ionizing photons have leaked from the young inner disk and that the ionizing spectrum has been hardened by intervening absorption ($\tau_{LL} \sim 3$ perpendicular to the disk). We adopt the atomic photoionization cross-section for which the average interstellar opacity varies as $E^{-2.43}$ above 13.6eV (Crudace *et al.* 1974). In quiescent galaxies, the outer HI disk is expected to have sub-solar metallicities (e.g., Molla *et al.* 1996). But the ongoing nuclear starburst in NGC 253 (Beck & Beckwith 1984; Antonucci & Ulvestad 1988) could conceivably enrich the outer disk through long-range galactic fountains (Corbelli & Salpeter 1988). On balance, we adopt solar abundances (Grevesse & Anders 1989) modified by the known depletion rates for cold gas (Cowie & Songaila 1986; Jenkins 1987; Savage & Massa 1987).

Gas phase depletion. The formation of grains depletes primarily Ca, Fe and Si which in turn suppresses the dominant coolants from the singly-ionized stages of these atoms (Ferland 1992). For example, at $U = 10^{-4}$, [CII]158 μm and [SII]35 μm account for one quarter of the total nebular cooling. While C, N and O are not strongly depleted, the forbidden line emission from N^+ , O° , O^+ and O^{++} is greatly enhanced by the increased temperature. In particular, Mathis (1986) finds that the [NII]/ $\text{H}\alpha$ ratio increases as $T_e^{3.6}$. Therefore, a 20% increase in the local electron temperature can effectively double this line ratio. We neglect grain heating and cooling processes (Reynolds & Cox 1992) as these are only important in the high U limit (Baldwin *et al.* 1991; Ferland 1992). Complete removal of the grain population from the depleted gas causes line strengths to change by no more than 5% (Shields 1992).

Photoionization models. In Fig. 9, we show the detailed ionization and thermal structure within the gaseous slab. N° , O° and H° are closely coupled with slight differences due to charge exchange reactions. N^+ , O^+ and H^+ are therefore also closely linked, except that divergence can occur at the front of the slab if the radiation field is sufficiently strong to produce a higher state of ionization in N or O. The soft photons are soaked up and fully ionize the front of the slab; the harder photons propagate further into the gas and set up a partially ionized zone. Here, the electron temperature increases by 25% which boosts the emissivities of the [OI], [OII], [NII] and [SII] lines. The high energy photons are essential: cutting off the continuum just below the ionization potential of NII (29.6 eV) produces [NII] λ 6548/ $\text{H}\alpha$ line ratios no higher than 0.25.

Fig. 10 shows the dependence of five important line diagnostics on both ionization parameter and the gas column density. The range of column densities shown are relevant to spiral edges. The line ratio [NII] λ 6583/ $\text{H}\alpha$ peaks at $U = 10^{-4}$ with a fivefold enhancement when compared with HII regions. In the warped disk model above, we expect $\phi = 3 - 30 \times 10^4 \text{ phot cm}^{-2} \text{ s}^{-1}$. Only the high end of this range is sufficient to explain the $\text{H}\alpha$ recombination emission. For a gas disk with a thickness of 1 kpc, $\mathcal{E}_m = 0.1 \text{ cm}^{-6} \text{ pc}$ implies $n_e \approx 0.01 \text{ cm}^{-3}$, such that for a fully ionized gas, $U = 10^{-5} - 10^{-4}$. The high end of this range is indeed where the [NII] λ 6548/ $\text{H}\alpha$ ratio peaks in Fig. 10. The observed ratio ([NII] λ 6548/ $\text{H}\alpha \approx 1$) implies [NII] λ 6583/ $\text{H}\alpha$ (≈ 3) is a factor of two higher than the peak of the curve in Fig. 10. While this model may have some application to the HI edges of NGC 253, a full explanation of the gas excitation requires an additional heat source.

Our attempt to explain the enhanced [NII]/ $\text{H}\alpha$ ratios with the dilute, hardened radiation field is made

much more difficult if the particle column density seen from the nucleus is much less than 3×10^{19} atoms cm^{-2} . It is noteworthy that $[\text{OI}]\lambda 6300$ is produced deep within the slab compared to $[\text{OII}]$ and $[\text{OIII}]$. The relative strength of these lines exhibits a complex interdependence on the shape of the ionizing spectrum, the ionization parameter and, most crucially, the column density of the ionized gas. Fig. 10 illustrates that, in fact, all emission lines exhibit some dependence on the gas column density.

Rand (1997) emphasizes the importance of the $\text{He I } \lambda 5876/\text{H}\alpha$ and the $[\text{NII}]/\text{H}\alpha$ ratios, taken together, for constraining the He ionizing fraction and the ionizing spectrum. Domgörgen & Mathis (1994) predict a high He ionizing fraction if the enhanced $[\text{NII}]$ emission is due to a dilute, hardened radiation field. A direct measurement of the kinetic temperature is possible from a detection of the $[\text{NII}]\lambda 5755$ line (Osterbrock 1989). But these V band lines are expected to be an order of magnitude fainter than $\text{H}\alpha$ which puts them at the limit of detectability (BTVS).

Finally, we summarize the steps that were taken to achieve the enhanced low ionization line ratios in Fig. 10. If $[\text{NII}]\lambda 6583/\text{H}\alpha = 0.3$ is typical for a high U model (e.g. HII region), a dilute radiation field ($U < 0.01$) in the neighbourhood of hot stars can double this ratio (e.g. Mathis 1986). Hardening the dilute radiation field with interstellar absorption can produce line ratios closer to unity (e.g. Sokolowski 1991). An additional 50% increase is achieved with the known gas phase depletions of refractory elements. Further enhancement of this ratio (for a fixed abundance) requires that we selectively heat the electrons without producing a higher ionization state of nitrogen.

7. Conclusions

We have succeeded in detecting ionized gas at and beyond the HI cut-off radius in the nearby spiral galaxy, NGC 253. This galaxy is a member of a small ensemble, the Sculptor group, with a low internal dispersion and little or no associated hot medium. The detected emission measures of the $\text{H}\alpha$ and $[\text{NII}]$ lines are sufficiently strong that it is unlikely the source of the ionization is the metagalactic UV background. The strength of the $[\text{NII}]$ line with respect to the $\text{H}\alpha$ line argues for an enhanced electron temperature at large galactic radius compared with the inner HII regions. The dominant ionization mechanism is suspected to be due to hot young stars in the inner regions which see the warped outer HI disk. We present a composite ionization model which may have some application to the HI edges of NGC 253, but a full explanation requires additional heat sources. The kinematic measurements confirm that the rotation curve is still rising at and beyond the HI edge. In some respects, since the HI disk ceases to be detectable at only $1.2 R_{25}$, this is not an ideal object for testing the original proposal of Bochkarev & Sunyaev (1977). But there are a few objects which subtend a large solid angle on the sky and have HI disks extending to beyond $2R_{25}$: these are the focus of subsequent papers.

JBH wishes to thank Oxford University for a Visiting Fellowship and for their hospitality during the preparation of this manuscript. We acknowledge extended dialogues with Dennis Sciama, Jon Weisheit and James Binney. We are indebted to Walter Dehnen for his insights, and for carrying out a least-squares fit to our data. Both an anonymous referee and the Scientific Editor, G.D. Bothun, made substantive comments which improved the presentation of this manuscript. Keith Taylor and Sylvain Veilleux assisted in some of the observations and the etalon was loaned to us by Brent Tully. We acknowledge comments from George Field communicated by Dennis Sciama. JBH wishes to thank Jim Sokolowski for permission to reproduce unpublished work arising from extensive collaborations.

REFERENCES

- Adams, F.C. & Laughlin, G. 1996, ApJ, 468, 586
- Antonucci, R.R.J. & Ulvestad, J.S. 1988, ApJ, 330, L97
- Arp, H. 1985, AJ, 90, 1012
- Bahcall, J.N. *et al.* 1991, ApJ, 377, L5
- Baldwin, J. *et al.* 1991, ApJ, 374, 580
- Beck, S.C. & Beckwith, S.V. 1984, MNRAS, 207, 671
- Benjamin, R.A. & Shapiro, P.R. 1993, In *The Evolution of Galaxies and their Environment*, NASA Ames publ., p. 338
- Bica, E. & Alloin, D. 1987, A&A, 70, 281
- Bland-Hawthorn, J. 1997, PASA, in press
- Bland-Hawthorn, J., Ekers, R.D., van Breugel, W., Koekemoer, A. & Taylor, K. 1995, ApJ, 447, L77
- Bland-Hawthorn, J. & Maloney, P.R. 1997, ApJ, in press
- Bland-Hawthorn, J., Taylor, K., Veilleux, S. & Shopbell, P.L. 1994, ApJ, 437, L95
- Bochkarev, N.G. & Sunyaev, R.A. 1977, Soviet Astr. 21, 542 (originally 1975, AZh, 54, 957)
- Boggs, P.T., Byrd, R.H. & Schnabel, R.B. 1987, SIAM J. Sci. & Stat. Computing, 8(6), 1052
- Bosma, A. 1978, University of Groningen thesis.
- Bowyer, S. 1991, ARAA, 29, 59
- Carignan, C. 1985, ApJ, 299, 59
- Carignan, C. 1991, Proc. Workshop on Dark Matter, Space Telescope Sci. Inst.
- Carignan, C. & Freeman, K.C. 1985, 294, 494
- Chabrier, G., Segretain, L. & M'era, D. 1996, ApJ, 468, L21
- Charlot, S. & Silk, J. 1995, ApJ, 445, 124
- Corbelli, E. & Salpeter, E.E. 1988, ApJ, 326, 551
- Corbelli, E., Schneider, S.E. & Salpeter, E.E. 1989, AJ, 97, 390
- Cowie, L.L. & Songaila, A. 1986, ARAA, 24, 499
- Crudace, R. *et al.* 1974, ApJ, 187, 497
- Dehnen, W. & Binney, J. 1997, MNRAS, in press
- Diaz, A.I. 1989, in *Evolutionary Phenomena in Galaxies*, eds. J.E. Beckman & B.E.J. Pagel (Cambridge: Cambridge University Press), 377
- Domgögen, H. & Mathis, J.S. 1994, ApJ, 428, 647
- Dopita, M.A. & Sutherland, R. 1996, ApJS, 102, 161
- Dove, J.B. & Shull, J.M. 1994, ApJ, 423, 196
- Draine, B.T. & Lee, H.M. 1984, ApJ, 285, 89
- Evans, N. & Dopita, M.A. 1985, ApJS, 58, 125

- Fadda *et al.* 1996, ApJ, 473, 670
- Ferland, G. & Mushotsky, R. 1984, ApJ, 286, 42
- Ferland, G. & Netzer, H. 1983, ApJ, 264, 105
- Ferland, G. 1991, Cloudy code, OSU Internal report, 91-01
- Ferland, G. 1992, ApJ, 389, L63
- Freeman, K.C. 1993, in *Physics of Nearby Galaxies: Nature or Nurture*, ed Trinh Thuan *et al.* (Paris: Editions Frontieres), p 201.
- Freeman, K.C. 1996, in *Unsolved Problems of the Milky Way*, ed L. Blitz and P. Teuben (Dordrecht: Kluwer), p 645.
- Grevesse, N. & Anders, E. 1989, In *Cosmic Abundances of Matter*, (New York: AIP), p. 1
- Haardt, F. & Madau, P. 1996, ApJ, 461, 20
- Halpern, J.P. & Steiner, J.E. 1983, ApJ, 269, L37
- Haynes, M.P. & Roberts, M.S. 1979, ApJ, 227, 767
- Heney, L.G. & Greenstein, J.L. 1941, ApJ, 93, 70
- Henry, R.C. 1991, ARAA, 29, 89
- Hogan, C.J. & Weymann, R.J. 1987, MNRAS, 225, 1P
- Jenkins, E.B. 1987, in *Interstellar Processes*, eds. D.J. Hollenbach & H.A. Thronson (Dordrecht: Reidel), 533
- Jura, M. 1980, ApJ, 241, 965
- Kawaler, S. 1996, ApJ, 467, L61
- Kamphuis, J. 1993, PhD, Groningen
- Kondratyev, K. Ya. 1969, in *Radiation in the Atmosphere*, Academic Press, New York & London
- Koribalski, B., Whiteoak, J.B. & Houghton, S. 1995, PASA, 12, 20
- Kurucz, R.L. 1979, ApJS, 40, 1
- Lee, Y.-W. 1993, In *The Globular Cluster-Galaxy Connection*, eds. G.H. Smith & J.P. Brodie, ASP. conf. ser. 48, 142
- Liebert, J., Dahn, C.C. & Monet, D.G. 1988, ApJ, 332, 891
- Lyon, J.G. 1975, ApJ, 201, 168
- Bania, T.M. & Lyon, J.G. 1980, ApJ, 239, 173
- Maeder, A. 1990, A&AS, 84, 139
- Malin, D.F. 1981, J. Phot. Sci., 29, 199
- Malin, D.F. 1983, In *Astronomy with Schmidt-type Telescopes*, ed. M Capaccioli, IAU Coll. 78, 57 (Reidel: Dordrecht)
- Maloney, P. 1993, ApJ, 414, 41
- Martin, P.G. & Rouleau, F. 1990, preprint
- Mathewson, D.S. & Ford, V.L. 1984, In *Structure & Evolution of the Magellanic Clouds* (Reidel: Dordrecht), IAU Symp. 108, 125

- Mathewson, D.S., Cleary, M.N. & Murray, J.D. 1975, ApJ, 195, L97
- Mathis, J. 1986, ApJ, 301, 423
- Mathis, J., Ruml, W. & Nordsieck, K.H. 1977, ApJ, 217, 425
- Mihalas, D. 1972, Non-LTE Model Atmospheres for B & O stars (NCAR-TN/STR-76)
- Miller, G.E. & Scalo, J.M. 1979, ApJS, 41, 513
- Molla, M., Ferrini, F. & Diaz, A.I. 1996, ApJ, 466, 668
- Nordgren, T.E., Cordes, J.M. & Terzian, Y. 1992, AJ, 104, 1465
- Olling, R.P. 1995, 110, 591
- Osterbrock, D.E. & Martel, A. 1992, PASP, 104, 76
- Osterbrock, D.E. 1989, Astrophysics of Gaseous Nebulae & Active Galactic Nuclei, Univ. Sci. Books
- Pagal, B.E.J. 1989, in Evolutionary Phenomena in Galaxies, eds. J.E. Beckman & B.E.J. Pagal (Cambridge: Cambridge University Press), 201
- Puche, D. & Carignan, C. 1991, ApJ, 378, 487
- Puche, D., Carignan, C. & van Gorkom, J. 1991, AJ, 101, 456
- Rand, R. 1997, ApJ, 474, 129
- Raymond, J. 1990, ApJ, 365, 387
- Reynolds, R.J. & Cox, D.P. 1992, ApJ, 400, L33
- Rots, A.H. 1975, A&A, 45, 43
- Ryder, S. *et al.* 1996, PASA, 14, 81
- Ryu, D., Olive, K.A. & Silk, J. 1990, ApJ, 353, 81
- Salucci, P. & Frenck, C.S. 1989, MNRAS, 237, 247
- Salpeter, E.E. 1955, ApJ, 121, 161
- Sargent, W.L.W. & Steidel, C.C. 1990, in Baryonic Dark Matter, eds. D. Lynden-Bell & G. Gilmore (Dordrecht: Kluwer), 223
- Savage, B.D. & Massa, D. 1987, ApJ, 314, 380
- Schommer, R. *et al.* 1993, AJ, 105, 97
- Sciama, D.W. 1995, MNRAS, 276, L1
- Sciama, D.W. 1996, Modern Cosmology & The Dark Matter Problem (Cambridge: Cambridge Univ. Press)
- Shields, J.C. 1992, ApJ, 339, L27
- Slavin, J.D., Shull, J.M. & Begelman, M.C. 1993, ApJ, 407, 83
- Smith, G.P. 1963, Bull. Astron. Inst. Neth., 17, 203
- Sokolowski, J. 1994, preprint (unpubl.)
- Sokolowski, J. & Bland-Hawthorn, J. 1991, PASP, 103, 911
- Spyromilio, J. 1995, MNRAS, 277, L59
- Staveley-Smith, L. *et al.* 1990, ApJ, 364, 23
- Sutherland, R.S. & Dopita, M.A. 1993, ApJS, 88, 253

- Tarter, C.B., Tucker, W.H. & Salpeter, E.E. 1969, *ApJ*, 156, 943
- van Albada, T.S., Bahcall, J.N., Begeman, K. & Sancisi, R. 1985, *ApJ*, 295, 305
- van Gorkom, J. 1993, In *Environment & Evolution of Galaxies*, eds. J.M. Shull & H.A. Thronson (Kluwer: Dordrecht), p. 345
- Veilleux, S. 1988, PhD thesis, U. C. Santa Cruz
- Vogel, S.N., Weymann, R., Rauch, M. & Hamilton, T. 1995, *ApJ*, 441, 162
- Wakker, B.P. 1991, *AA&AS*, 90, 495
- Wood, P. 1990, *JRASC*, 84, 150
- Yelle, R.V. & Roesler, F. 1985, *JGR*, 90, 7568
- Zaritsky, D., Smith, R., Frenk, C., & White, S.D.M. 1997, *ApJ*, 478, 39

FIGURE CAPTIONS

Fig. 1. TAURUS-2 5' fields (SW1, SW2, SW3, SW4) superimposed on a B image of NGC 253. The blue [NII] line occurs at smaller galaxian radii compared with the $H\alpha$ line in the same field. There are four distinct fields with two emission lines occurring in each. At the central position, the etalon was used at two different spacings which meant that we obtained line detections at four discrete positions.

Fig. 2. Same as Fig. 1 except that the TAURUS-2 fields have been superimposed onto a deep ATNF HI map (Koribalski, Whiteoak & Houghton 1995). The outermost HI contour corresponds to a column density of $4 \times 10^{18} \text{ cm}^{-2}$.

Fig. 3. A magnified image of part of the SW3 field in Figs. 1 and 2. The field of view is rotated so that the vertical axis lies parallel to the galaxy major axis. Clumpy [NII] and $H\alpha$ emission is clearly visible. What is not easily rendered is the diffuse emission between and at large off-axis angles to the major axis. Notice the extremely faint galaxy continuum ($B \sim 25 \text{ mag arcsec}^{-2}$) over much of the field. The bright arcs are atmospheric OH lines.

Fig. 4. The emission-line spectrum at the HI edge (Field SW3 in Figs. 1 and 2) compared with the off-field spectrum. The difference of these spectra is shown below. Remarkably, the [NII] $\lambda 6548$ line has a surface brightness comparable to the $H\alpha$ surface brightness, as compared with solar-abundance HII regions where the ratio is an order of magnitude smaller. This result holds after removing the dense knots in Fig. 3. The azimuthally averaged galaxy continuum underlies the spectrum and corresponds to roughly $\mu_B = 23 \text{ mag arcsec}^{-2}$ below [NII] falling to $25 \text{ mag arcsec}^{-2}$ below $H\alpha$. The equivalent widths of the lines are 0.60\AA and 1.8\AA respectively.

Fig. 5. The emission-line spectrum for the field beyond the HI edge (Field SW4 in Figs. 1 and 2). As we did not get a matching sky exposure, the spectra are shown from binning over two different opening angles. The top spectrum results from binning over 25° about the major axis from the optical axis; the lower spectrum arises from binning over the entire field. The difference of these spectra is shown below. The [NII] emission is clearly seen in the top spectrum and, indeed, in a high contrast image. This line is completely washed out in the lower spectrum. The $H\alpha$ emission is just visible in the high contrast image, and does not begin to appear until we sum over the entire field. The difference has been taken after weighting the top spectrum for its lower signal to noise ratio. Again, we see a very faint galaxy continuum spectrum which is roughly $\mu_B = 26 \text{ mag arcsec}^{-2}$ after azimuthal binning below the [NII] line dropping to $\mu_B = 27 \text{ mag arcsec}^{-2}$ below the $H\alpha$ line. The equivalent widths of the lines are 7.8\AA and 9.9\AA respectively.

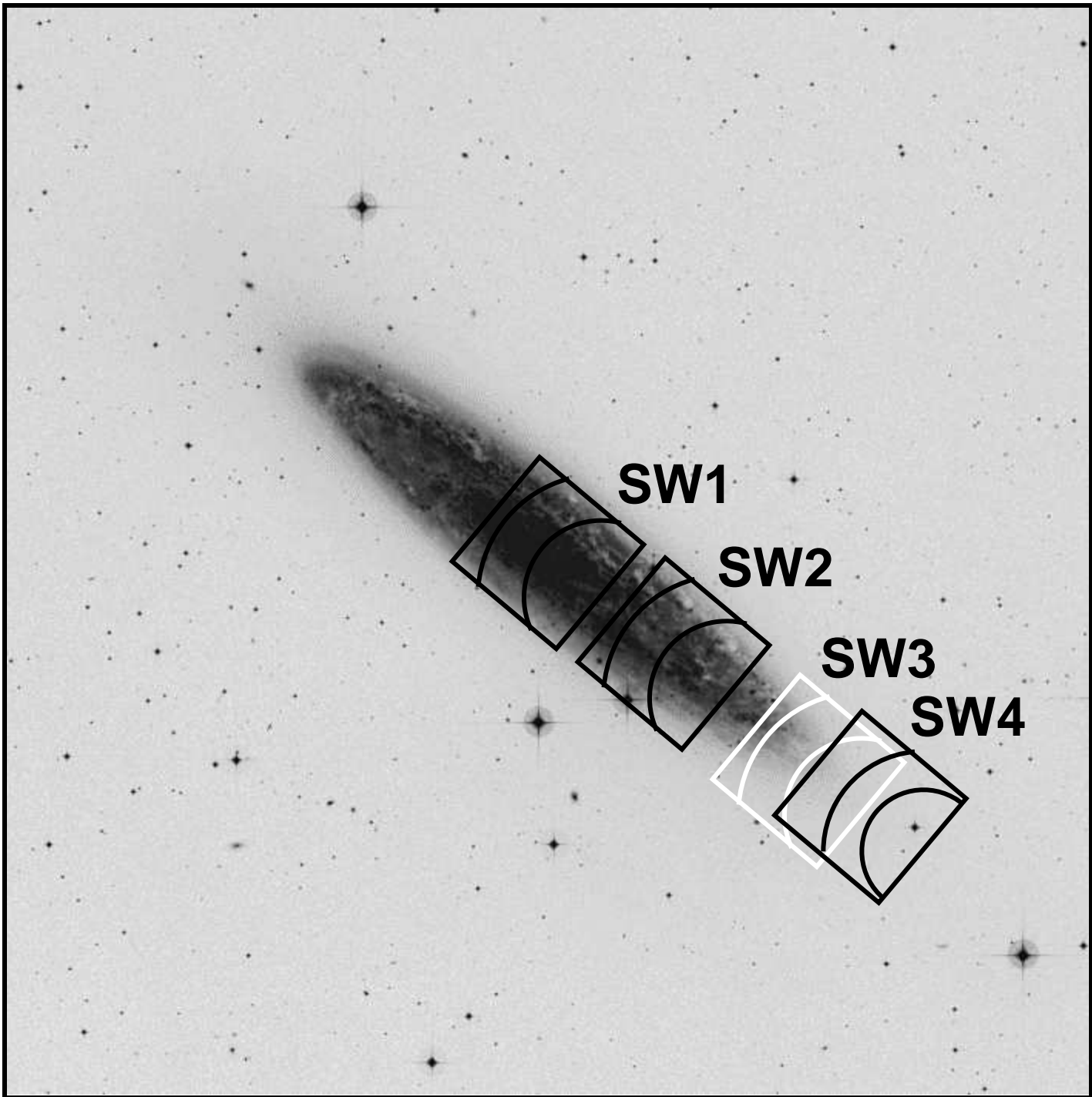
Fig. 6. Kinematic measurements along the major axis of NGC 253 deduced from VLA HI, TAURUS-2 $H\alpha$ and [NII] lines. In *a*, the original rotation curve of PCvG has been projected onto the sky with their inferred orbit inclination at each radius. Three sets of measurements are shown: these represent the approaching side (open circles), receding side (squares), and from fitting to the full velocity field (filled circles). In *b*, we show PCvG's original curves where the data have been deprojected with the measured inclination at each radius. In *c*, the solid line is the same curve as the squares in *a*. The filled squares are the TAURUS-2 [NII] measurements; the circles are the $H\alpha$ measurements.

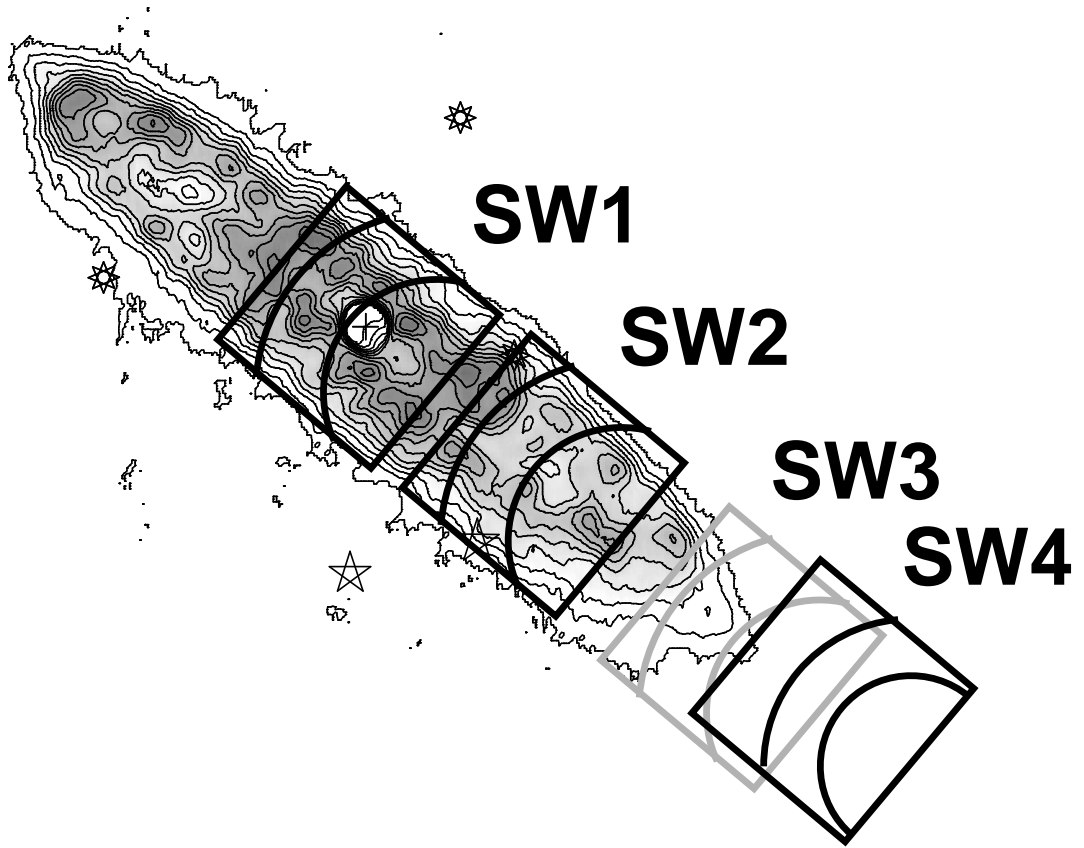
Fig. 7. Representative fits to the PCvG and TAURUS-2 data using a 3-component mass model (disk, halo, gas). The contribution from the HI surface density (dotted line) is the same in all models. In *a*, we adopt an exponential disk (short-dashed line) and choose an isothermal sphere for the spherical halo (long-dashed line) using the numerical approach developed by Carignan (1985). In *b*, we have used the disk-halo models of Dehnen & Binney (1997): the least-squares fit was carried out by W. Dehnen. In *c*, we have truncated the halo at a radius of 10 kpc to demonstrate a possible explanation for the last measured point.

Fig. 8. The predicted $H\alpha$ emission measure \mathcal{E}_m versus B surface brightness for an isothermal population of white dwarfs as a function of surface density. The solid lines are isotherms for white dwarf temperatures in the range $10^4 - 2 \times 10^5$ K. The dashed lines are isochoric lines indicating variations in white dwarf surface density in steps of 0.5 in dex starting at 1 pc^{-2} at the top. The arrow indicates the average emission measure and disk surface brightness upper limit at the edge of the HI disk. The filled circles are the expected contribution to the B band flux and $H\alpha$ emission measure for the white dwarf population in the solar neighbourhood (assuming that all photons are absorbed). The Galactic disk is assumed to be 600 pc thick and the white dwarf radius is assumed to be $0.14 R_\odot$.

Fig. 9. The lower panel shows the relative ionization fraction of important neutrals and ions, where the front of the gas slab ($N_H = 0$) is ionized by a dilute radiation field ($U \sim 10^{-4}$). The middle panel shows the temperature and mean electron density structure within the slab. The top panel shows the normalized line emissivities and illustrates the relative dependence on electron temperature, electron density, and ionization fraction.

Fig. 10. The dependence of five important line diagnostics on the strength of the radiation field and hydrogen column density. The solid lines are radiation bounded models where all ionizing photons are soaked up by the gas. Also shown are matter bounded models where the slab has been truncated at 1, 2, 5, 10 and $20 \times 10^{18} \text{ cm}^{-2}$. The observed line ratio $[\text{NII}]\lambda 6548/H\alpha$ is a factor of 2.98 smaller than $[\text{NII}]\lambda 6583/H\alpha$ (Veilleux 1988). Fig. 9 gives some appreciation for the distinct trends shown by different lines (e.g. $[\text{OI}]$ vs. $[\text{OIII}]$).

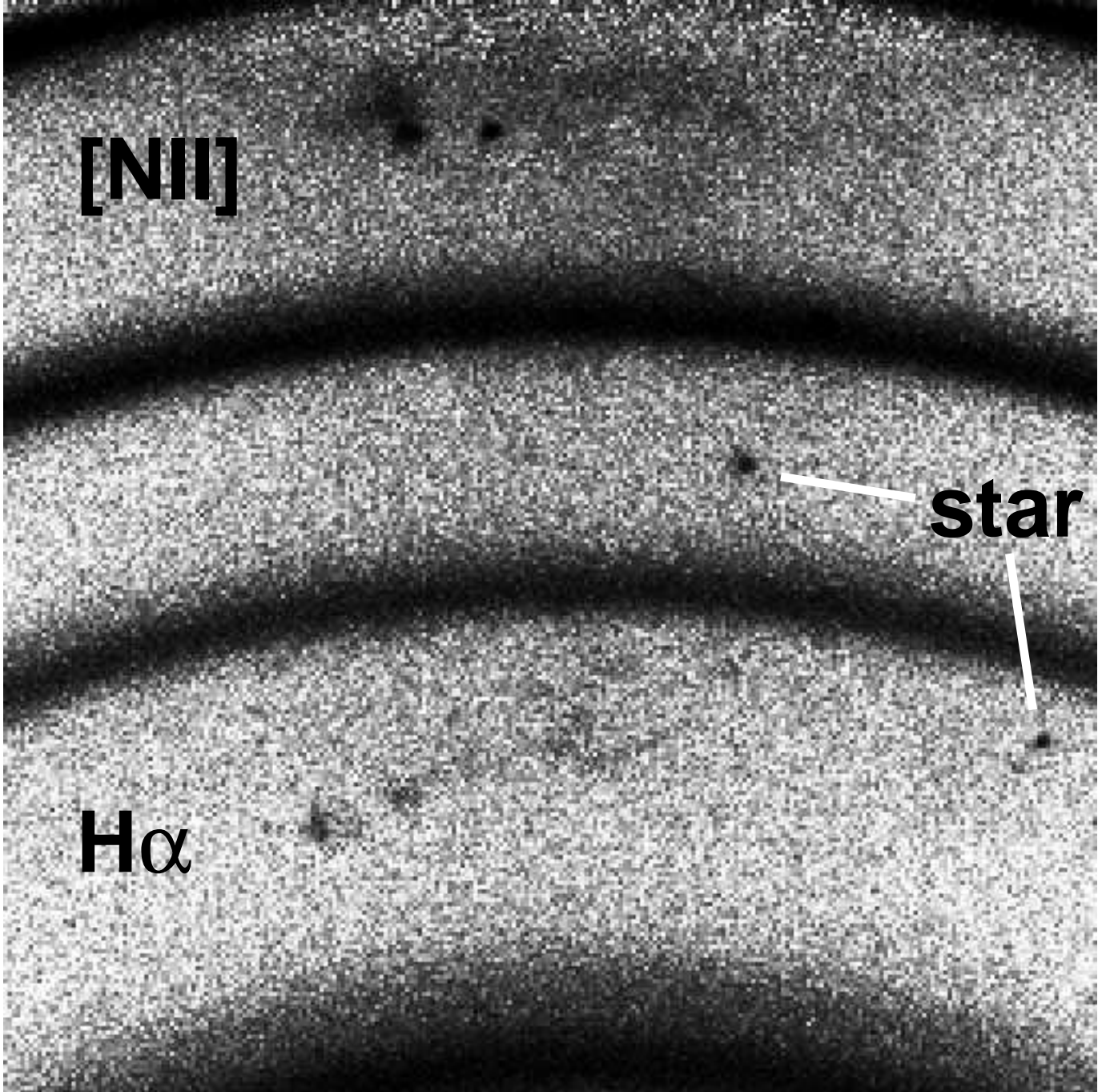


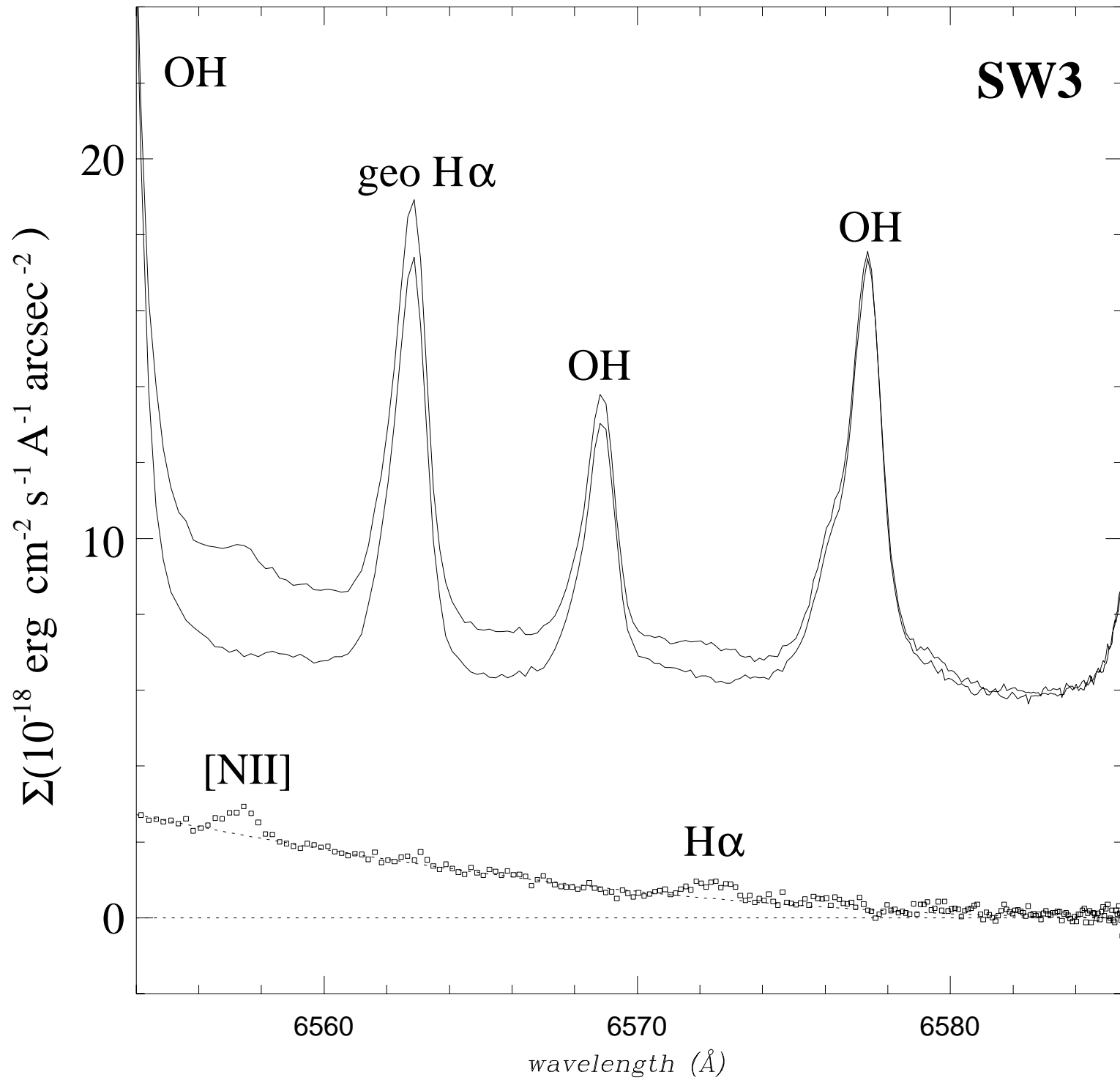


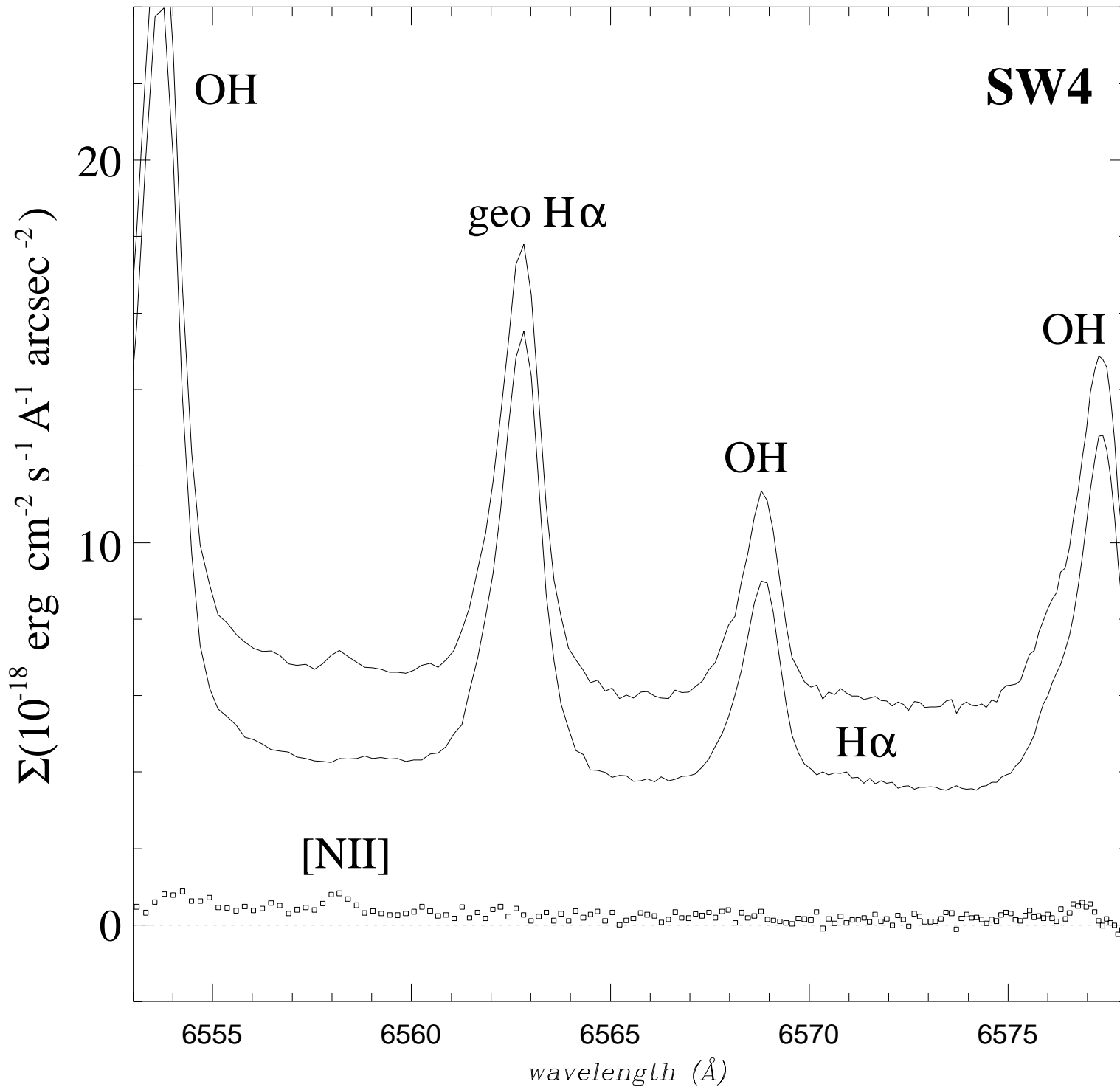
[NII]

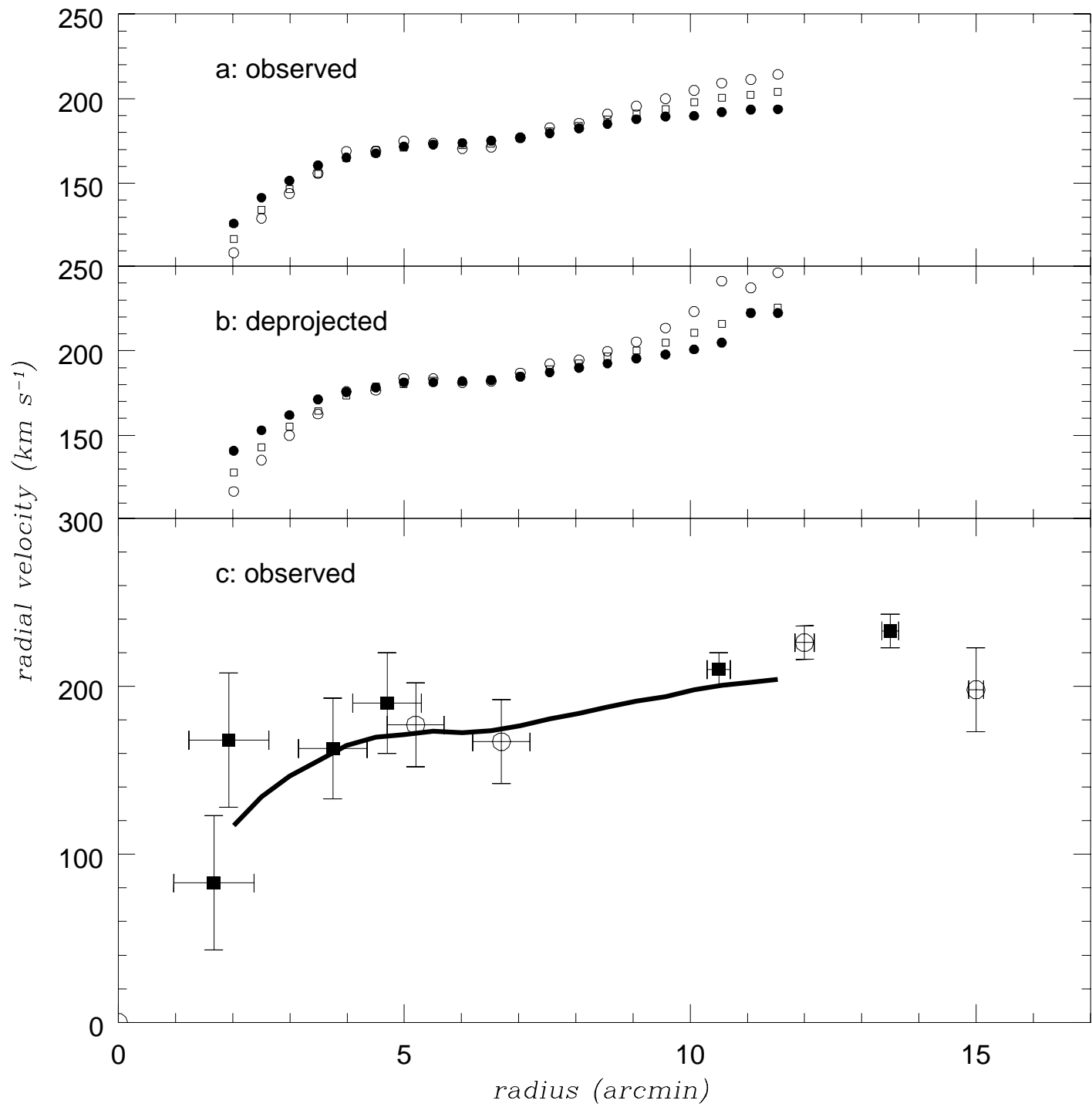
star

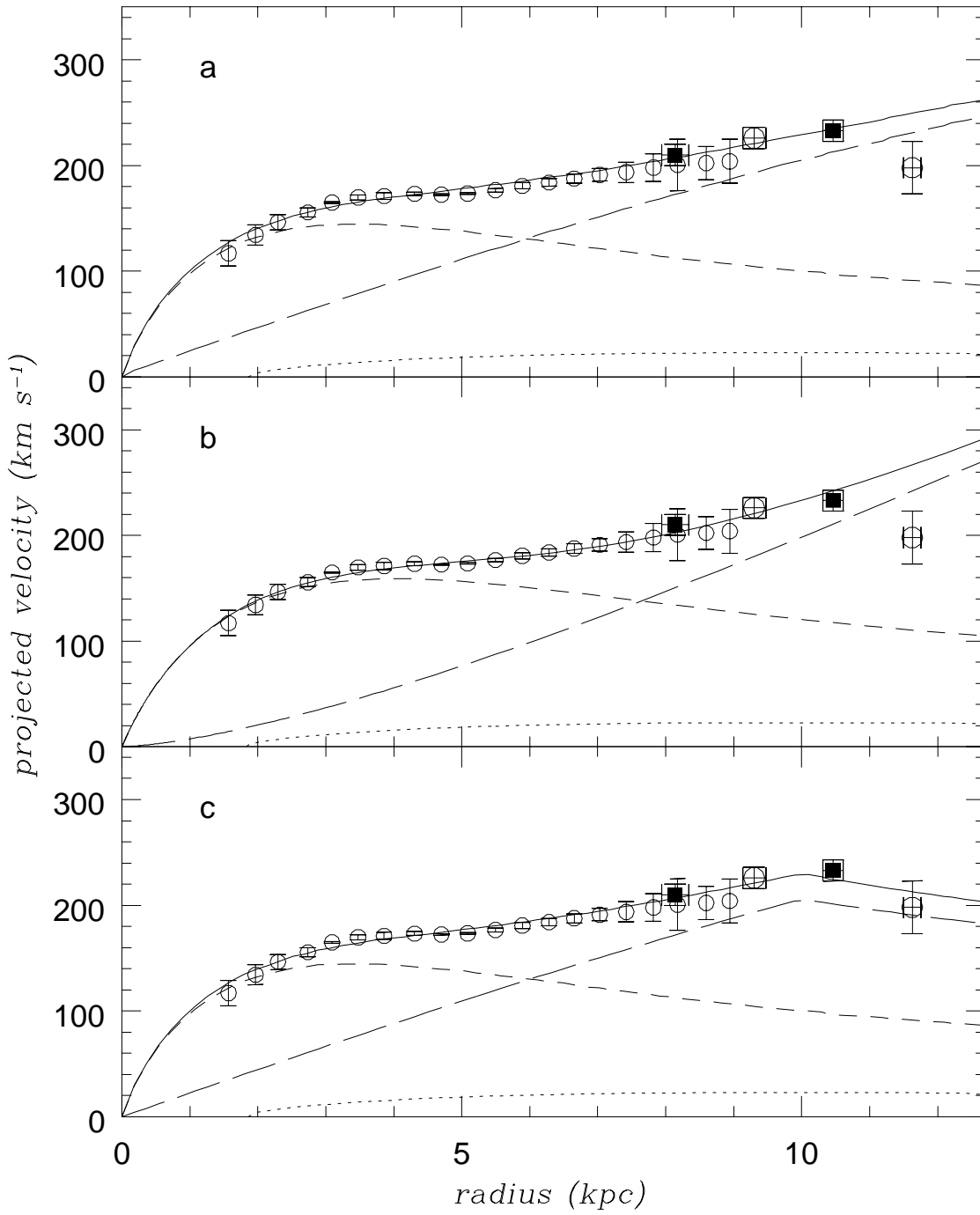
H α

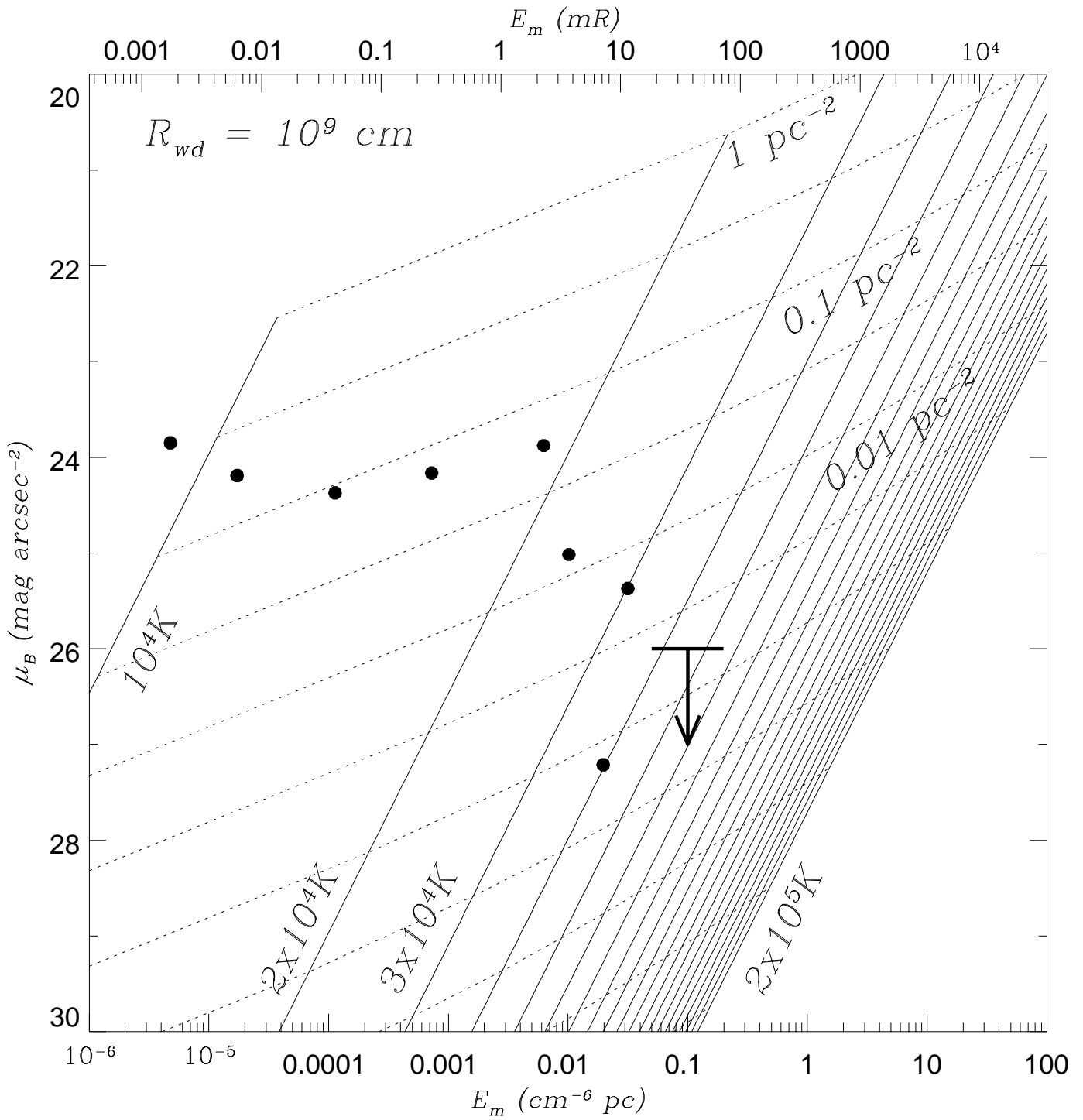


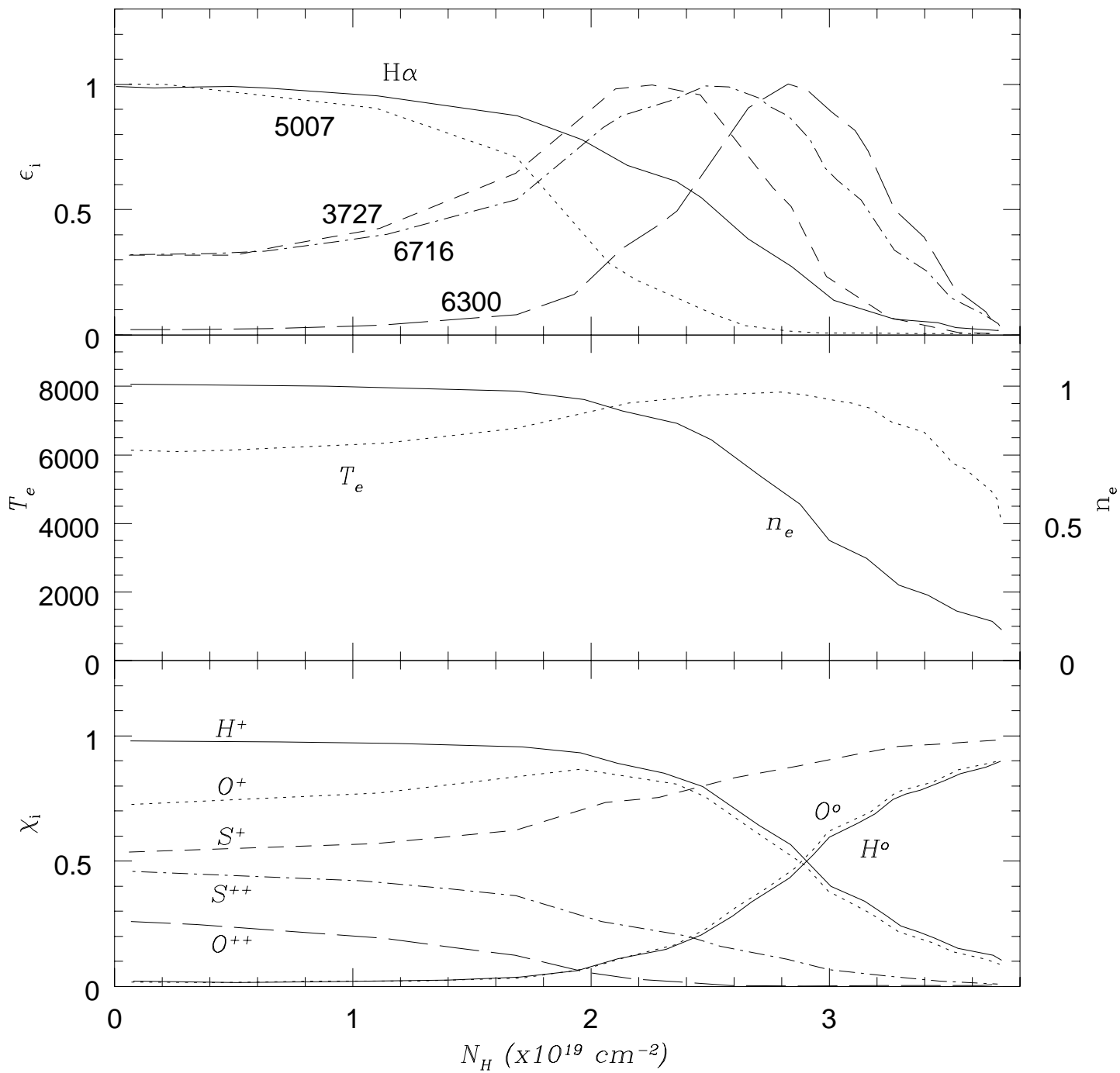


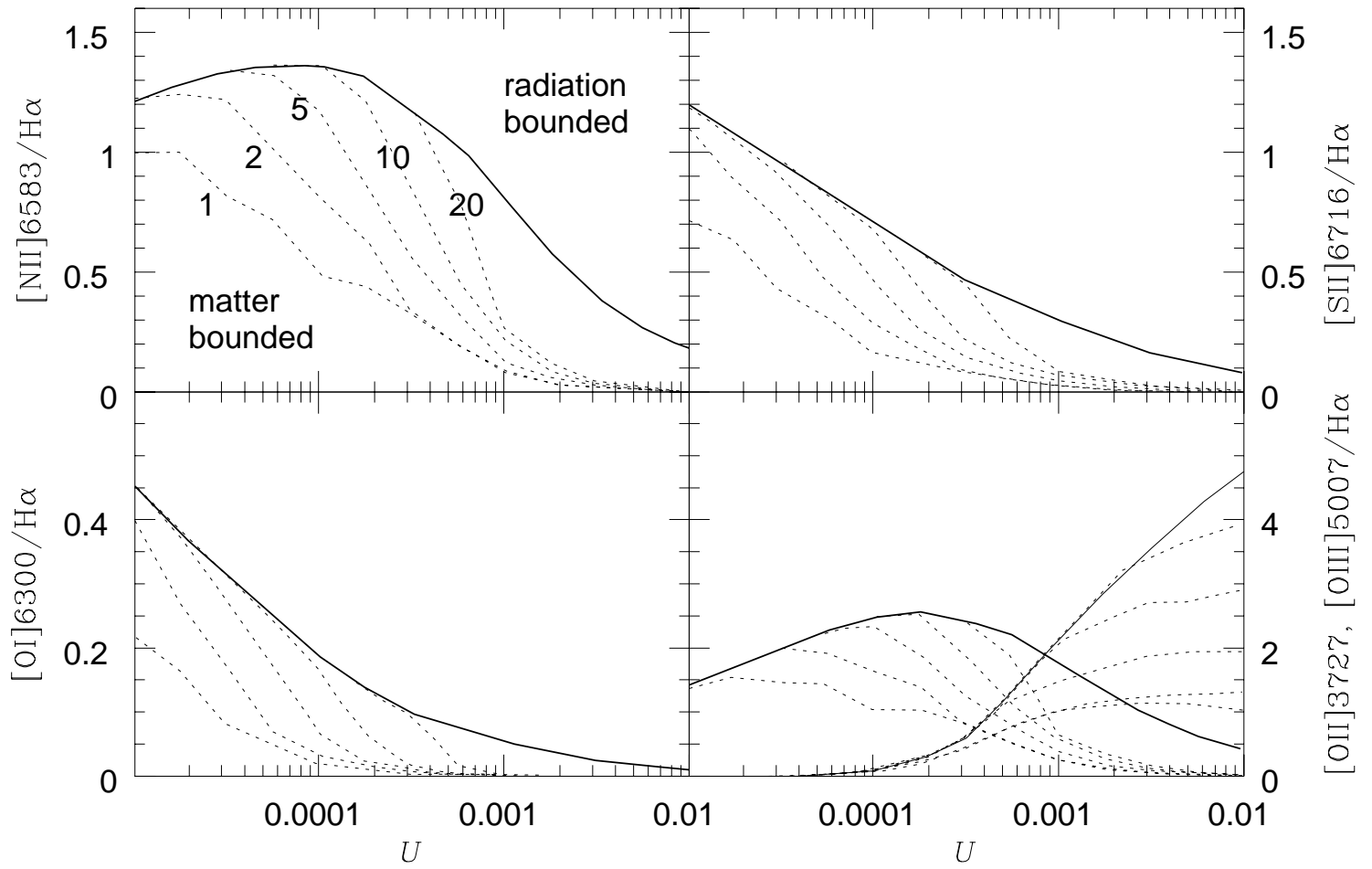












Object	focus	exposures	date	filter	gap	airmass	seeing	P.A.
<i>Flux standard: line</i>								
N6072	f/8	6 min	9/8/94	6555/45/0	...	1.1	1.0	0
N6302	f/8	6 min	9/8/94	6555/45/0	...	1.1	1.3	0
N6445	f/8	6 min	10/8/94	6555/45/0	...	1.1	1.3	0
N6563	f/8	6 min	10/8/94	6555/45/0	...	1.1	1.3	0
<i>Flux standard: continuum</i>								
LTT 7379	f/8	3×1 min	9/8/94	6555/45/0	...	1.1	1.7	0
CD-32 9927	f/8	3×2 min	10/8/94	6555/45/0	...	1.1	1.3	0
HZ 7	f/15	2 min	27/9/95	6585/43/8	260	1.4	0.9	230
Hiltner 600	f/15	2 min	27/9/95	6585/43/8	260	1.3	0.9	230
<i>Blank fields</i>								
Sky #1	f/8	6×20 min	11/8/94	6555/45/0	180	1.3–1.9	1.4	230
Smith #1	f/8	6×20 min	9/8/94	6555/45/0	200	1.4	1.7	0
Smith #2	f/8	8×20 min	10/8/94	6555/45/0	200	1.4	1.3	0
Smith #2	f/8	5×20 min	11/8/94	6555/45/0	180	1.2–1.3	1.3	230
<i>Object fields</i>								
N253 #1 (SW1)	f/8	5 min	10/8/94	6555/45/0	200	1.7	1.3	230
N253 #2 (SW2)	f/8	10 min	10/8/94	6555/45/0	200	1.2	1.3	230
N253 #2 (SW2)	f/8	5 min	10/8/94	6555/45/0	260	1.2	1.3	230
N253 #3 (SW3)	f/8	18×20 min	10/8/94	6555/45/0	260	1–1.4	1.3	230
N253 #4 (SW4)	f/8	16×20 min	11/8/94	6555/45/0	240	1–1.9	1.5	230
N253 #3 (SW3)	f/15	2×20 min	27/9/95	6585/43/8	260	1.2–1.4	1.0	230
N253 #3 (SW3)	f/15	5×30 min	27/9/95	6585/43/8	260	1.4–1.6	0.9	230

NOTE.— (1) Object name (2) AAT focus (3) exposure times (4) local date of observation (5) blocking filter / bandwidth (Å) / tilt angle (6) etalon gap in BCV units (ellipsis indicates full FSR scanned) (7) average airmass (8) seeing disk FWHM (9) position angle of detector on the sky.